

# Pomeron, nucleon-resonance, and $(0^+, 0^-, 1^+)$ -meson contributions in $\phi$ -meson photoproduction

Sang-Ho Kim<sup>1,2,\*</sup> and Seung-il Nam<sup>2,3,†</sup>

<sup>1</sup>*Center for Extreme Nuclear Matters (CENuM), Korea University, Seoul 02841, Korea*

<sup>2</sup>*Department of Physics, Pukyong National University (PKNU), Busan 48513, Korea*

<sup>3</sup>*Asia Pacific Center for Theoretical Physics (APCTP), Pohang 37673, Korea*

(Dated: October 20, 2021)

We investigate the reaction mechanism of the  $\phi$ -meson photoproduction off the proton target, i.e.,  $\gamma p \rightarrow \phi p$ , up to  $\sqrt{s} = 2.8$  GeV. For this purpose, we employ an effective Lagrangian approach in the tree-level Born approximation, and we employ various experimental and theoretical inputs. As a theoretical setup, the vectorlike Pomeron ( $C = +1$ ) is taken into account as a parameterized two-gluon exchange contribution. We also consider  $f_1(1285)$  axial-vector-meson,  $(\pi, \eta)$  pseudoscalar-meson, and  $(a_0, f_0)$  scalar-meson exchanges in the  $t$  channel, in addition to the experimentally confirmed nucleon resonances, such as  $N^*(2000, 5/2^+)$  and  $N^*(2300, 1/2^+)$ , for the direct  $\phi$ -meson radiations in the  $s$  and  $u$  channels. We provide numerical results for the total and differential cross sections as well as the spin-density matrices in the Gottfried-Jackson, Adair, and helicity frames. We observe that, together with the universally accepted pomeron contribution, the considered meson and nucleon-resonance contributions play significant roles in reproducing the experimental data for the forward and backward  $\phi$ -meson scattering-angle regions, respectively, indicating the nontrivial interferences between mesonic and baryonic contributions.

PACS numbers: 13.60.Le, 13.40.-f, 14.20.Jn, 14.20.Gk

Keywords:  $\phi$ -meson photoproduction, Pomeron, axial-vector meson, nucleon resonance, effective Lagrangian approach.

arXiv:1904.05133v3 [hep-ph] 31 Dec 2019

---

\* E-mail: sangho.kim@korea.ac.kr

† E-mail: sinam@pknu.ac.kr

## I. INTRODUCTION

$\phi$ -meson photoproduction off the proton target, i.e.,  $\gamma p \rightarrow \phi p$ , has attracted a lot of interest especially, since the bump structure was observed at very forward-angle regions near the threshold in the experiment of the LEPS Collaboration [1]. Because the  $\phi$ -meson is characterized by the hidden strangeness, hyperon exchanges in the  $u$  channel are forbidden and nucleon-pole contributions in the  $s$  channel are also suppressed, due to the Okubo-Zweig-Iizuka (OZI) rule [2–4]. Thus, the reaction mechanism of the  $\phi$ -meson photoproduction is distinguished from those of the  $\rho$ - and  $\omega$ -meson photoproductions, resulting in its cross section being much smaller than others. It is also well known that diffractive Pomeron ( $\mathbb{P}$ ) exchange governs the monotonically increasing high-energy behavior of the cross section, but can not explain the bump structure near the threshold region  $\sqrt{s} = (2.0 - 2.2)$  GeV. Refs. [5, 6] interpret the bump structure as the coupled-channel effects between the  $\phi p$  and  $K^+\Lambda(1520)$  channels. Moreover, Refs. [7, 8] suggest a postulated spin-3/2 resonance with  $M_{N^*} \approx 2.1$  GeV and  $\Gamma_{N^*} \approx 500$  MeV to reproduce the bump.

Meanwhile, in 2014, the CLAS Collaboration at Jefferson Laboratory [9, 10] reported the first abundant data containing both the charged and neutral modes of the  $\phi \rightarrow K\bar{K}$  decay for the  $\phi$ -meson photoproduction. These high-statistics differential cross sections and spin-density matrix elements (SDMEs) data cover the energy range  $\sqrt{s} = (2.0 - 2.8)$  GeV and the full angular range beyond the very forward angle. They imply many interesting features: i) The local structure studied previously persists only in the forward angle regions and vanishes around the  $\phi$ -meson scattering angle  $\cos\theta \approx 0.8$  in the center-of-mass (c.m.) frame. Then, two bumplike structures are shown again at backward angles  $\cos\theta = -(0.4 - 1.0)$  near  $\sqrt{s} \approx 2.1$  and 2.3 GeV, although the magnitudes of the cross sections are far more suppressed than those at forward angles. ii) The comparison of the differential cross sections between the charged ( $\phi \rightarrow K^+K^-$ ) and neutral ( $\phi \rightarrow K_S^0 K_L^0$ ) modes [10] offers the best chance to extract the re-scattering effect between the  $\phi p$  and  $K^+\Lambda(1520)$  channels, because the neutral mode excludes the  $\Lambda(1520) \rightarrow pK^-$  final state configuration. The similarity between these two modes implies that the re-scattering effect and the interference are marginal. The bump structure at  $\sqrt{s} \approx 2.2$  GeV is also clearly seen in the both modes. Moreover, the LEPS Collaboration [11] subsequently confirmed that the  $\sqrt{s} \approx 2.2$  GeV structure is regardless of the  $\phi$ - $\Lambda(1520)$  interference effects in the  $\gamma p \rightarrow K^+K^-p$  reaction. Keeping these in mind, other reaction processes should come into play essentially [12]. iii) The SDME  $\rho_{00}^0$  provides us with the information of helicity conservation between the initial photon and the final  $\phi$  meson, because it is proportional to the squares of the two helicity-flip amplitudes. Nonzero values of  $\rho_{00}^0$  are observed in the three different reference frames, i.e., the Gottfried-Jackson, Adair, and helicity ones, resulting in violation of both  $t$ -channel helicity conservation and  $s$ -channel helicity conservation. In this regard, it is of great importance to carry out a systematical analysis of the  $\phi$ -meson photoproduction.

In the present work, we investigate the reaction mechanism of the  $\phi$ -meson photoproduction with an effective Lagrangian approach in the tree-level Born approximation. To take into account the spatial distributions of hadrons involved, well-established phenomenological form factors are considered as well. We take into account the exchanges of the vectorlike Pomeron ( $\mathbb{P}$ ), the  $f_1(1285)$  axial-vector (AV) meson, the  $(\pi, \eta)$  pseudoscalar (PS) mesons, and the  $(a_0, f_0)$  scalar (S) mesons in the  $t$ -channel Feynman diagram. The general argument about the  $\phi$ -meson photoproduction is that the conventional Pomeron exchange governs even at low energies and meson exchanges are suppressed, because the OZI rule [2] puts constraints on direct exchanges of quarks for the  $\gamma\mathbb{P}\phi$  vertex. By the analysis of the world CLAS data on the  $\phi$ -meson photoproduction, we can readily test, to what extent of energies, the Pomeron exchange has its effect on the cross sections and SDMEs. The relative contributions of the AV, PS, and S mesons also can be verified. In addition, the direct  $\phi$ -meson radiations are considered in the  $s$  and  $u$  channels, through the ground-state nucleon and its resonances.

Among the nucleon resonances given in the Particle Data Group (PDG) [13], we include  $N^*(2000, 5/2^+)$  and  $N^*(2300, 1/2^+)$ , which are located near the  $\phi N$  threshold. We find that they are the most essential for describing the CLAS data, instead of other scenarios such as a single hypothetical resonance [5, 7, 8], meson-baryon box-shape loop contributions [6], and the interference of the  $\phi$  meson with  $\Lambda(1520)$  via  $\gamma p \rightarrow K^+K^-p$  [11]. We face some difficulty owing to the lack of information about the  $N^* \rightarrow \phi N$  decays of the PDG resonances, while their photo-excitations  $\gamma N \rightarrow N^*$  are relatively well known. We extract the branching ratios for  $N^* \rightarrow \phi N$  by fitting to the CLAS data and compare them with those for the open-strangeness  $N^* \rightarrow K^*\Lambda$  decays recently reported by the PDG [13].

This paper is organized as follows: In Sec. II, we present detailed explanations for the theoretical framework. Section III is devoted to the numerical results of cross sections and SDMEs and the relevant discussions. The summary is given in Sec. IV. The details of the invariant amplitudes, SDMEs, and three reference frames are given in the appendixes.

## II. THEORETICAL FRAMEWORK

In this section, we provide the theoretical framework to study the  $\phi$ -meson photoproduction off the proton target  $\gamma(k_1) + p(p_1) \rightarrow \phi(k_2) + p(p_2)$ . We employ an effective Lagrangian approach and the tree-level Feynman diagrams under consideration are depicted in Fig. 1. The Reggeized two-gluon exchange, i.e., the Pomeron ( $\mathbb{P}$ ), is taken into account in the  $t$  channel to describe the slowly rising total cross section with respect to the beam energy [Fig. 1(a)]. Exchanges of the  $f_1(1285)$  AV,  $(\pi, \eta)$  PS, and  $(a_0, f_0)$  S mesons are considered in the  $t$  channel [Fig. 1(b)]. The direct  $\phi$ -meson radiations in the  $s$  and  $u$  channels via the proton and its resonances are also available [Figs. 1(c) and 1(d)]. In what follows, the explicit forms of the effective Lagrangians are explained for describing various hadron interactions for each Feynman diagram.

### A. Vectorlike Pomeron exchange

The effective Lagrangians for Pomeron exchange for the photon-Pomeron- $\phi$ -meson vertex can be written as [14, 15]

$$\mathcal{L}_{\gamma\mathbb{P}\phi} = ig_{\gamma\mathbb{P}\phi} F_\phi(t) [(\phi_\nu \partial^\mu \mathbb{P}^\nu - \mathbb{P}_\nu \partial^\mu \phi^\nu) A_\mu - (A_\nu \partial^\mu \mathbb{P}^\nu - \mathbb{P}_\nu \partial^\mu A^\nu) \phi_\mu - (\phi_\nu \partial^\mu A^\nu - A_\nu \partial^\mu \phi^\nu) \mathbb{P}_\mu], \quad (1)$$

where,  $\mathbb{P}^\mu$ ,  $A^\mu$ , and  $\phi^\mu$  indicate the  $C = +1$  vector like Pomeron, photon, and  $\phi$ -meson fields, respectively. Considering its vector like nature, the interaction of the Pomeron with the nucleon is casted into

$$\mathcal{L}_{\mathbb{P}NN} = g_{\mathbb{P}NN} F_N(t) \bar{N} \gamma_\mu N \mathbb{P}^\mu. \quad (2)$$

Here,  $N$  stands for the nucleon field. We define the strength  $C_{\mathbb{P}}$  for convenience by  $C_{\mathbb{P}} = g_{\gamma\mathbb{P}\phi} g_{\mathbb{P}NN}$ . The form of the invariant amplitude derived from Eqs. (1) and (2) is similar to that used in the Donnachie-Landshoff (DL) model [14–16] given in Appendix A. In this work, we employ the DL model for the Pomeron exchange process. The complicated two-gluon exchange calculation is simplified by the DL model which suggests that the Pomeron couples to the nucleon like a  $C = +1$  isoscalar photon and its couplings is described in terms of a nucleon isoscalar electromagnetic (EM) form factor  $F_N(t)$ . Figure 2 draws the quark diagram for this Reggeized Pomeron exchange. In Refs. [17, 18], the quark-loop integration in Fig. 2 is performed in connection with the DL model and can be approximated to the factorized form given by Donnachie and Landshoff [16] for the low energy region  $\sqrt{s} < 5$  GeV, justifying the application of the DL model to the present work.

The form factor for the  $\gamma\mathbb{P}\phi$  vertex [ $F_\phi(t)$ ] [19, 20] and the  $F_N(t)$  [21, 22] read

$$F_\phi(t) = \frac{2\mu_0^2}{(1 - t/\Lambda_\phi^2)(2\mu_0^2 + \Lambda_\phi^2 - t)}, \quad F_N(t) = \frac{4M_N^2 - a_N^2 t}{(4M_N^2 - t)(1 - t/t_0)^2}, \quad (3)$$

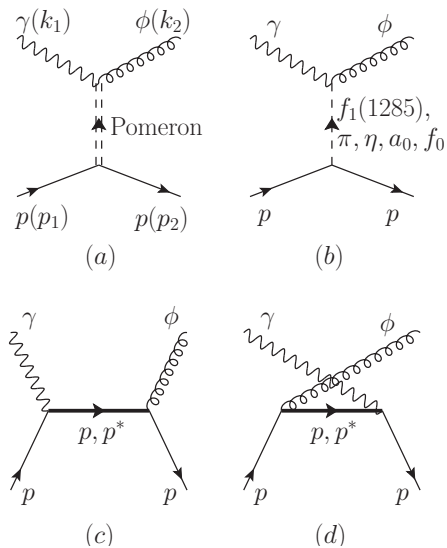


FIG. 1. Relevant Feynman diagrams for  $\gamma p \rightarrow \phi p$ , which include Pomeron (a), pseudoscalar  $(\pi, \eta)$ -meson, scalar  $(a_0, f_0)$ -meson, and axial-vector [ $f_1(1285)$ ]-meson exchanges in the  $t$  channel (b), and direct  $\phi$ -meson radiations via the proton and its resonances in the  $s$  and  $u$  channels (c and d). We define the four momenta for the involved particles as well.

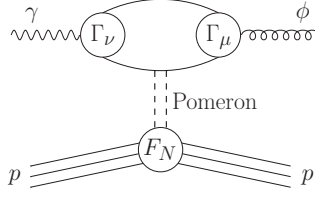


FIG. 2. Quark diagram for Pomeron exchange in the DL model.

respectively, where the scale parameters are given by  $\mu_0^2 = 1.1 \text{ GeV}^2$ ,  $a_N^2 = 2.8$ , and  $t_0 = 0.71 \text{ GeV}^2$ . The mass scale  $\Lambda_\phi$  is proportional to the quark mass of the loop diagram in Fig. 2 and is chosen to be  $\Lambda_\phi^2 = 4M_\phi^2$  which is rather larger than that given in Refs. [14, 15, 20] where  $\Lambda_\phi^2 = M_\phi^2$  is used. This modification makes the differential cross sections milder under the variations of the scattering angle  $\cos \theta$ . The Pomeron trajectory reads

$$\alpha_{\mathbb{P}}(t) = 1 + \epsilon_{\mathbb{P}} + \alpha'_{\mathbb{P}} t, \quad (4)$$

where the slope and intercept of the trajectory are determined to be  $\alpha'_{\mathbb{P}} = 0.25 \text{ GeV}^{-2}$  and  $\epsilon_{\mathbb{P}} = 0.08$  which is favored among  $0.08 - 0.12$  [22].

### B. $f_1(1285)$ axial-vector exchange

The  $f_1(1285)$  meson exchange is suggested in proton-proton scattering and vector meson photoproduction due to its special relation to the axial anomaly through the matrix elements of the flavor singlet axial vector current. Its Regge trajectory is expected to contribute to the large-energy and large-momentum transfer regions with an intercept of  $\alpha(0) \approx 1$  and a slope of  $\alpha' \approx 0$  as the odd-signature partner of the even signature Pomeron [23].

The effective Lagrangian for the  $AVV$  vertex is obtained by using the hidden gauge approach [24]:

$$\mathcal{L}_{\gamma\phi f_1} = g_{\gamma\phi f_1} \epsilon^{\mu\nu\alpha\beta} \partial_\mu A_\nu \partial^\lambda \partial_\lambda \phi_\alpha f_{1\beta}, \quad (5)$$

where  $f_1$  indicates the  $f_1(1285)$  field with its quantum number  $I^G(J^{PC}) = 0^+(1^{++})$ . The coupling constant  $g_{\gamma\phi f_1}$  can be calculated from the relation

$$\Gamma_{f_1 \rightarrow \phi\gamma} = \frac{k_\gamma^3}{12\pi} \frac{M_\phi^2}{M_{f_1}^2} (M_{f_1}^2 + M_\phi^2) g_{\gamma\phi f_1}^2, \quad (6)$$

derived from Eq. (5), where  $k_\gamma = (M_{f_1}^2 - M_\phi^2)/(2M_{f_1})$ , and the experimental data on the  $f_1$ -meson branching ratio (Br)  $\text{Br}_{f_1 \rightarrow \phi\gamma} = 7.5 \times 10^{-4}$  with  $\Gamma_{f_1} = 22.7 \text{ MeV}$  [13]:

$$g_{\gamma\phi f_1} = 0.17 \text{ GeV}^{-2}. \quad (7)$$

The axial-vector meson and nucleon interaction Lagrangian reads

$$\mathcal{L}_{f_1 NN} = -g_{f_1 NN} \bar{N} \left[ \gamma_\mu - i \frac{\kappa_{f_1 NN}}{2M_N} \gamma_\nu \gamma_\mu \partial^\nu \right] f_1^\mu \gamma_5 N, \quad (8)$$

where the coupling constant  $g_{f_1 NN}$  is not well known, and we use the maximum value

$$g_{f_1 NN} = 3.0, \quad (9)$$

with  $g_{f_1 NN} = 2.5 \pm 0.5$ , discussed in Ref. [25]. Although the tensor term can contribute to the  $\phi$ -meson photoproduction, we set the value of  $\kappa_{f_1 NN}$  to be zero in this calculation for brevity.

We reggeize the Feynman amplitude derived from Eqs. (5) and (8) (see Appendix A) by replacing the Feynman propagator by the Regge propagator, which effectively interpolates between small- and large-momentum transfer regions, such that the mesons of higher spin  $J = 3, 5, \dots$  in the same trajectory can contribute to the high energy region [26]

$$P_{f_1}^{\text{Feyn}}(t) = \frac{1}{t - M_{f_1}^2} \rightarrow P_{f_1}^{\text{Regge}}(t) = \left( \frac{s}{s_{f_1}} \right)^{\alpha_{f_1}(t)-1} \frac{\pi \alpha'_{f_1}}{\sin[\pi \alpha_{f_1}(t)]} \frac{1}{\Gamma[\alpha_{f_1}(t)]} D_{f_1}(t), \quad (10)$$

where the energy-scale factor is fixed to be  $s_{f_1} = 1 \text{ GeV}^2$  and the odd signature factor is given by

$$D_{f_1}(t) = \frac{\exp[-i\pi\alpha_{f_1}(t)] - 1}{2}. \quad (11)$$

The slope of the  $f_1(1285)$  trajectory is chosen to be  $\alpha'_{f_1} \approx 0.028 \text{ GeV}^{-2}$ , which is distinguished from that of the Pomeron because of its different characteristic scale relative to the Pomeron [23]. The intercept of the  $f_1(1285)$  trajectory is determined to be  $\alpha_{f_1}(0) = 0.99 \pm 0.04$  [23], which is rather larger than those of other vector and axial-vector meson trajectories [27].

### C. Pseudoscalar- and scalar-meson exchanges

The EM interaction Lagrangians for the PS- and S-meson exchanges, respectively, read

$$\begin{aligned} \mathcal{L}_{\gamma\Phi\phi} &= \frac{eg_{\gamma\Phi\phi}}{M_\phi} \epsilon^{\mu\nu\alpha\beta} \partial_\mu A_\nu \partial_\alpha \phi_\beta \Phi, \\ \mathcal{L}_{\gamma S\phi} &= \frac{eg_{\gamma S\phi}}{M_\phi} F^{\mu\nu} \phi_{\mu\nu} S, \end{aligned} \quad (12)$$

where  $\Phi = \pi^0(135, 0^-)$  and  $\eta(548, 0^-)$ , and  $S = a_0(980, 0^+)$  and  $f_0(980, 0^+)$ .  $e$  stands for the unit electric charge. The EM and  $\phi$ -meson field strengths are denoted by  $F^{\mu\nu} = \partial^\mu A^\nu - \partial^\nu A^\mu$  and  $\phi^{\mu\nu} = \partial^\mu \phi^\nu - \partial^\nu \phi^\mu$ , respectively. The relevant coupling constants are calculated from the widths of the  $\phi \rightarrow \Phi\gamma$  and  $\phi \rightarrow S\gamma$  radiative decays as follows:

$$\Gamma_{\phi \rightarrow \Phi\gamma} = \frac{\alpha}{3} \frac{q_\gamma^3}{M_\phi^2} g_{\gamma\Phi\phi}^2, \quad \Gamma_{\phi \rightarrow S\gamma} = \frac{4\alpha}{3} \frac{q_\gamma^3}{M_\phi^2} g_{\gamma S\phi}^2, \quad (13)$$

where  $\alpha = e^2/(4\pi)$  and  $q_\gamma = (M_\phi^2 - M_{\Phi,S}^2)/(2M_\phi)$ . The  $\phi$ -meson branching ratios are experimentally known to be  $\text{Br}_{\phi \rightarrow \pi\gamma} = 1.30 \times 10^{-3}$ ,  $\text{Br}_{\phi \rightarrow \eta\gamma} = 1.303 \times 10^{-2}$ ,  $\text{Br}_{\phi \rightarrow a_0\gamma} = 7.6 \times 10^{-5}$ , and  $\text{Br}_{\phi \rightarrow f_0\gamma} = 3.22 \times 10^{-4}$  [13], from which we obtain

$$g_{\gamma\pi\phi} = -0.14, \quad g_{\gamma\eta\phi} = -0.71, \quad g_{\gamma a_0\phi} = -0.77, \quad g_{\gamma f_0\phi} = -2.44, \quad (14)$$

with  $\Gamma_\phi = 4.249 \text{ MeV}$ .

The strong interaction Lagrangians for the PS- and S-meson exchanges are written as

$$\begin{aligned} \mathcal{L}_{\Phi NN} &= -ig_{\Phi NN} \bar{N} \Phi \gamma_5 N, \\ \mathcal{L}_{SNN} &= -g_{SNN} \bar{N} S N, \end{aligned} \quad (15)$$

respectively. We use the pseudoscalar meson-baryon coupling scheme rather than the pseudovector one for the former one in Eq. (15). They are equivalent to each other because the relevant two nucleons are on mass-shell. The following strong coupling constants are obtained by using the Nijmegen potentials [28, 29]:

$$g_{\pi NN} = 13.0, \quad g_{\eta NN} = 6.34, \quad g_{a_0 NN} = 4.95, \quad g_{f_0 NN} = -0.51, \quad (16)$$

which are also close to the values from the SU(3) flavor symmetry or the unitary symmetry except for  $g_{a_0 NN}$  [14].

We use the following parametrization of the form factors for the PS- and S-meson exchanges:

$$F_{\Phi,S}(t) = \frac{\Lambda_{\Phi,S}^2 - M_{\Phi,S}^2}{\Lambda_{\Phi,S}^2 - t}, \quad (17)$$

where  $\Lambda_{\Phi,S}$  denotes the cutoff masses, which will be determined to reproduce experimental data.

### D. Direct $\phi$ -meson radiation term

The effective Lagrangians for the direct  $\phi$ -meson radiation contributions are defined by

$$\begin{aligned} \mathcal{L}_{\gamma NN} &= -e\bar{N} \left[ \gamma_\mu - \frac{\kappa_N}{2M_N} \sigma_{\mu\nu} \partial^\nu \right] N A^\mu, \\ \mathcal{L}_{\phi NN} &= -g_{\phi NN} \bar{N} \left[ \gamma_\mu - \frac{\kappa_{\phi NN}}{2M_N} \sigma_{\mu\nu} \partial^\nu \right] N \phi^\mu, \end{aligned} \quad (18)$$

where the anomalous magnetic moment of the proton is given by  $\kappa_p = 1.79$ . The vector and tensor coupling constants for the  $\phi$ -meson to the nucleon are chosen to be  $g_{\phi NN} = -0.24$  and  $\kappa_{\phi NN} = 0.2$  [30]. Note that the corresponding individual invariant amplitudes, given by  $\mathcal{M}_{\phi \text{ rad}, s}$  and  $\mathcal{M}_{\phi \text{ rad}, u}$  in Eq. (39) in the Appendix A, violate the Ward-Takahashi identity (WTI). When we sum the electric terms of the two invariant amplitudes, the WTI is restored as a pair. Thus one needs a specific prescription for the usage of the phenomenological form factors. Detailed explanations for this can be found in Refs. [31–35]. We define the form factor as follows:

$$F_N(x) = \frac{\Lambda_N^4}{\Lambda_N^4 + (x - M_N^2)^2}, \quad x = (s, u), \quad (19)$$

and we take the common form factor which conserves the on-shell condition for the form factors [34] as

$$F_c(s, u) = 1 - [1 - F_N(s)][1 - F_N(u)], \quad (20)$$

for the electric terms. Because the magnetic terms satisfy the WTI by themselves, we just use the form of Eq. (19).

### E. Nucleon resonances

There are 11 nucleon resonances beyond the  $\phi N$  threshold  $\sqrt{s_{\phi N}} = 1.96$  GeV in the PDG data [13]:  $N^*(2000, 5/2^+)$ ,  $N^*(2060, 5/2^-)$ ,  $N^*(2100, 1/2^+)$ ,  $N^*(2120, 3/2^-)$ ,  $N^*(2190, 7/2^-)$ ,  $N^*(2220, 9/2^+)$ ,  $N^*(2250, 9/2^-)$ ,  $N^*(2300, 1/2^+)$ ,  $N^*(2570, 5/2^-)$ ,  $N^*(2600, 11/2^-)$ , and  $N^*(2700, 13/2^+)$  with their two-, three-, or four-star confirmations. Whereas the helicity amplitudes of  $N^* \rightarrow N\gamma$  transitions are well known for the nucleon resonances less than 2.3 GeV, the information of  $N^* \rightarrow \phi N$  strong decay is very limited for all PDG nucleon resonances. None of the  $N^* \rightarrow \phi N$  decay is observed firmly experimentally [13]. And the CLAS data for the differential cross sections exhibit two bumplike structures at the pole positions  $\sqrt{s} \approx 2.1$  and 2.3 GeV in the backward-scattering regions [10]. Considering these observations, we avoid performing a  $\chi^2$  fit in this calculation and try to reproduce the available experimental data with only a few resonances. As is explained in the next section in detail, we find that selecting only  $N^*(2000, 5/2^+)$  and  $N^*(2300, 1/2^+)$  is good enough for this exploratory work. The nucleon resonances beyond 2.3 GeV and with higher spins, i.e.,  $J \geq 9/2$ , are automatically excluded.

The effective Lagrangians for the EM transitions of the nucleon resonances read [36, 37]

$$\begin{aligned} \mathcal{L}_{\gamma NN^*}^{1/2^\pm} &= \frac{eh_1}{2M_N} \bar{N}\Gamma^{(\mp)} \sigma_{\mu\nu} \partial^\nu A^\mu N^* + \text{H.c.}, \\ \mathcal{L}_{\gamma NN^*}^{5/2^\pm} &= e \left[ \frac{h_1}{(2M_N)^2} \bar{N}\Gamma_\nu^{(\mp)} - \frac{ih_2}{(2M_N)^3} \partial_\nu \bar{N}\Gamma^{(\mp)} \right] \partial^\alpha F^{\mu\nu} N_{\mu\alpha}^* + \text{H.c.}, \end{aligned} \quad (21)$$

for their spin and parity  $J^P$ , and we define the following notation for brevity:

$$\Gamma^{(\pm)} = \begin{pmatrix} \gamma^5 \\ I_{4 \times 4} \end{pmatrix}, \quad \Gamma_\mu^{(\pm)} = \begin{pmatrix} \gamma_\mu \gamma^5 \\ \gamma_\mu \end{pmatrix}. \quad (22)$$

$N^*$  and  $N_{\mu\alpha}^*$  stand for the Rarita-Schwinger spin-1/2 and -5/2 nucleon resonance fields, respectively [38]. The former one in Eq. (21) is constructed from the  $\gamma NN$  interaction in Eq. (18), but the electric term is removed to conserve the WTI. The Breit-Wigner helicities  $A_i$  for  $N^*(2000, 5/2^+)$  are given in the PDG data [13] by  $A_{1/2}^{N^*(2000) \rightarrow p\gamma} = 0.031$  and  $A_{3/2}^{N^*(2000) \rightarrow p\gamma} = -0.043$  [ $\text{GeV}^{-\frac{1}{2}}$ ] and we extract the EM transition coupling constants  $h_i$  in Eq. (21) [36, 39, 40] from these values:  $h_1^{N^*(2000)} = -4.24$  and  $h_2^{N^*(2000)} = 4.00$ .

The effective Lagrangians for the strong interactions can be expressed as

$$\begin{aligned} \mathcal{L}_{\phi NN^*}^{1/2^\pm} &= \pm \frac{1}{2M_N} \bar{N} \left[ \frac{g_1 M_\phi^2}{M_{N^*} \mp M_N} \Gamma_\mu^{(\mp)} \pm g_2 \Gamma_\mu^{(\mp)} \sigma_{\mu\nu} \partial^\nu \right] \phi^\mu N^* + \text{H.c.}, \\ \mathcal{L}_{\phi NN^*}^{5/2^\pm} &= \left[ \frac{g_1}{(2M_N)^2} \bar{N}\Gamma_\nu^{(\mp)} - \frac{ig_2}{(2M_N)^3} \partial_\nu \bar{N}\Gamma^{(\mp)} + \frac{ig_3}{(2M_N)^3} \bar{N}\Gamma^{(\mp)} \partial_\nu \right] \partial^\alpha \phi^{\mu\nu} N_{\mu\alpha}^* + \text{H.c.}, \end{aligned} \quad (23)$$

Here, only the first term  $g_1$  is considered to avoid additional ambiguities and the values of  $g_2$  and  $g_3$  are set to be zero. We determine the value of  $g \equiv g_1$  very carefully to reproduce the CLAS data, resulting in  $g_{N^*(2000)} = 4.0$ , and extract the corresponding branching ratio:  $\text{Br}_{N^*(2000) \rightarrow \phi N} = 1.5 \times 10^{-3}$ .

It is worth comparing the computed branching ratio  $\text{Br}_{N^* \rightarrow \phi N}$  with those for the open strangeness  $N^* \rightarrow K^* \Lambda$  decays. The recent Bonn-Gatchina partial wave analysis of the  $\gamma p \rightarrow K^{*+} \Lambda$  reaction derived them, where  $N^*(1895, 1/2^-)$ ,  $N^*(2000, 5/2^+)$ , and  $N^*(2100, 1/2^+)$  turn out to be dominant and other several ones also give  $N^* \rightarrow K^* \Lambda$  branching ratios with small but finite values [41]. We obtain

$$\frac{\text{Br}(N^*(2000) \rightarrow \phi N)}{\text{Br}(N^*(2000) \rightarrow K^* \Lambda)} \simeq 0.07. \quad (24)$$

For the case of  $N^*(2300, 1/2^+)$ , because its photo-coupling is unknown, a product of the EM and strong decay channels is taken into account to reproduce the data as follows:

$$\sqrt{\text{Br}_{N^*(2300) \rightarrow \phi N}} \times A_{1/2}^{N^*(2300) \rightarrow p \gamma} = 3.8 \times 10^{-3} \text{ GeV}^{-\frac{1}{2}}. \quad (25)$$

The full decay widths of the two nucleon resonances are chosen to be  $\Gamma_{N^*(2000)} = 200$  MeV and  $\Gamma_{N^*(2300)} = 300$  MeV.

Meanwhile, Refs. [42, 43] used an SU(3) quark model to probe the nucleon resonances that strongly couple to the  $\phi N$  channel. Reference [44] suggested the effect of the hidden-strangeness pentaquark state  $P_s^+ = s\bar{s}uud$  as its charmed partner, i.e., two exotic charmoniumlike states  $P_c^+(4312)$  and  $P_c^+(4450)$ , observed at the LHCb Collaboration [45, 46], are studied in the same  $s$ -channel diagram for the  $\gamma p \rightarrow J/\psi p$  photoproduction [47–50].

The Gaussian form factor is used because it is advantageous to suppress unreasonably-increasing cross sections with respect to  $\sqrt{s}$  for the  $N^*$  contributions [51–55]:

$$F_{N^*}(x) = \exp \left[ -\frac{(x - M_{N^*}^2)^2}{\Lambda_{N^*}^4} \right], \quad x = (s, u). \quad (26)$$

We observe that the contribution of the  $u$ -channel diagram of Fig. 1(d) is almost negligible and all the  $N^*$  contributions come from the  $s$ -channel diagram of Fig. 1(c).

### III. NUMERICAL RESULTS AND DISCUSSIONS

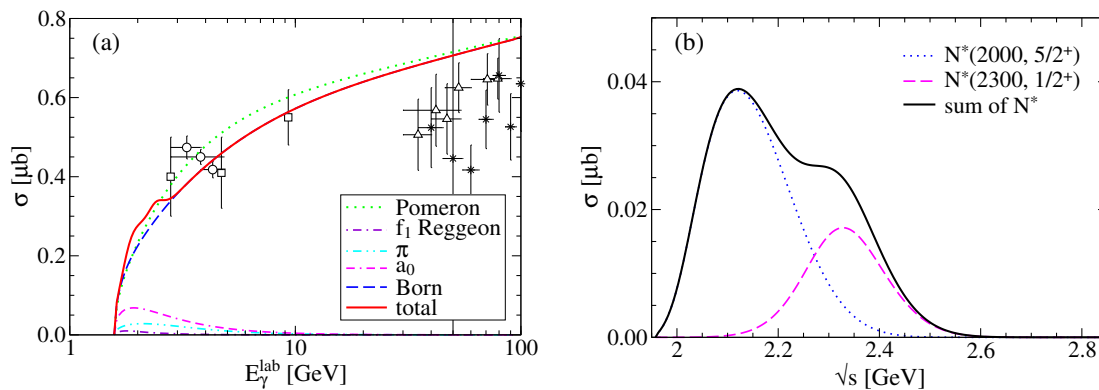


FIG. 3. (a) Total cross section is plotted as a function of the photon laboratory energy  $E_\gamma^{\text{lab}}$ . The data are taken from Refs. [56–59]. (b) Each contribution of the two nucleon resonances as a function of the c.m. energy  $\sqrt{s}$ .

We are now in a position to present the numerical results and relevant discussions. We first fix the strength factor for the Pomeron exchange to be  $C_{\mathbb{P}} = 6.5$  such that the formal  $s \rightarrow \infty$  asymptotic behavior of the total cross section is properly described. Then the low-energy CLAS data [9, 10] are used to constrain other model parameters: The cutoff masses for PS- and S-meson exchanges are fixed to be  $\Lambda_{\pi, \eta} = 0.87$  and  $\Lambda_{a_0, f_0} = 1.35$  GeV, respectively, and those for the  $\phi$ -meson radiations and  $N^*$  exchanges are fixed to be  $\Lambda_{N, N^*} = 1.0$  GeV. The unpolarized differential cross section can be expressed in terms of the invariant amplitudes as follows:

$$\frac{d\sigma}{d\Omega} = \frac{1}{64\pi^2 s} \frac{|\mathbf{q}|}{|\mathbf{k}|} \frac{1}{4} \sum_{\text{spins}} \left| \sum_{h=B, N^*} \mathcal{M}_h(F_h)^n \right|^2, \quad (27)$$

where  $\mathbf{k}$  and  $\mathbf{q}$  indicate the three-momenta of the incoming photon and the outgoing  $\phi$ -meson, respectively, defined in the c.m. frame. The exchanged particles are composed of the Born ( $B=\mathbb{P}, f_1(1285), \pi, \eta, a_0, f_0, N$ ) and nucleon-resonance [ $N^*=N^*(2000, 5/2^+), N^*(2300, 1/2^+)$ ] terms. As for the relevant phase factors between exchanged particles, the factor  $e^{i\pi/2}$  is additionally multiplied to the scalar exchange amplitude for a better description of the experimental data. We give the details of all the invariant amplitudes in Appendix A.

Figure 3(a) shows the total cross section for  $\gamma p \rightarrow \phi p$  as a function of the photon laboratory (lab) energy  $E_\gamma^{\text{lab}}$ . Although the present theoretical setup is not applicable to the higher-energy region far beyond the threshold, we plot the numerical results up to  $E_\gamma^{\text{lab}} = 100$  GeV to see the tendency of the curves. The conventional Pomeron exchange (green dotted curves) matches with the intermediate-energy data at  $E_\gamma^{\text{lab}} = (3 - 10)$  GeV [56, 57] but rather overestimates the data in the high-energy range  $E_\gamma^{\text{lab}} \gtrsim 30$  GeV [58, 59]. The strength of the Pomeron exchange is almost the same as that of the Born contribution. AV-, PS-, and S-meson exchanges have small effects on the total cross section but come into play significantly for the differential cross sections and spin-density matrix elements (SDMEs) as will be seen later. The  $\pi$ - and  $a_0$ -meson exchanges turn out to be more important than the  $\eta$ - and  $f_0$ -meson ones, respectively. The structure shown at  $E_\gamma^{\text{lab}} = (1.6 - 3.0)$  GeV comes from the contribution of the two nucleon resonances. Each and total  $N^*$  contributions are shown in Fig. 3(b) as a function of the c.m. energy  $\sqrt{s}$ .  $N^*(2100, 5/2^+)$  and  $N^*(2300, 1/2^+)$  are responsible for the peaks around  $\sqrt{s} \approx 2.1$  and 2.3 GeV, respectively.

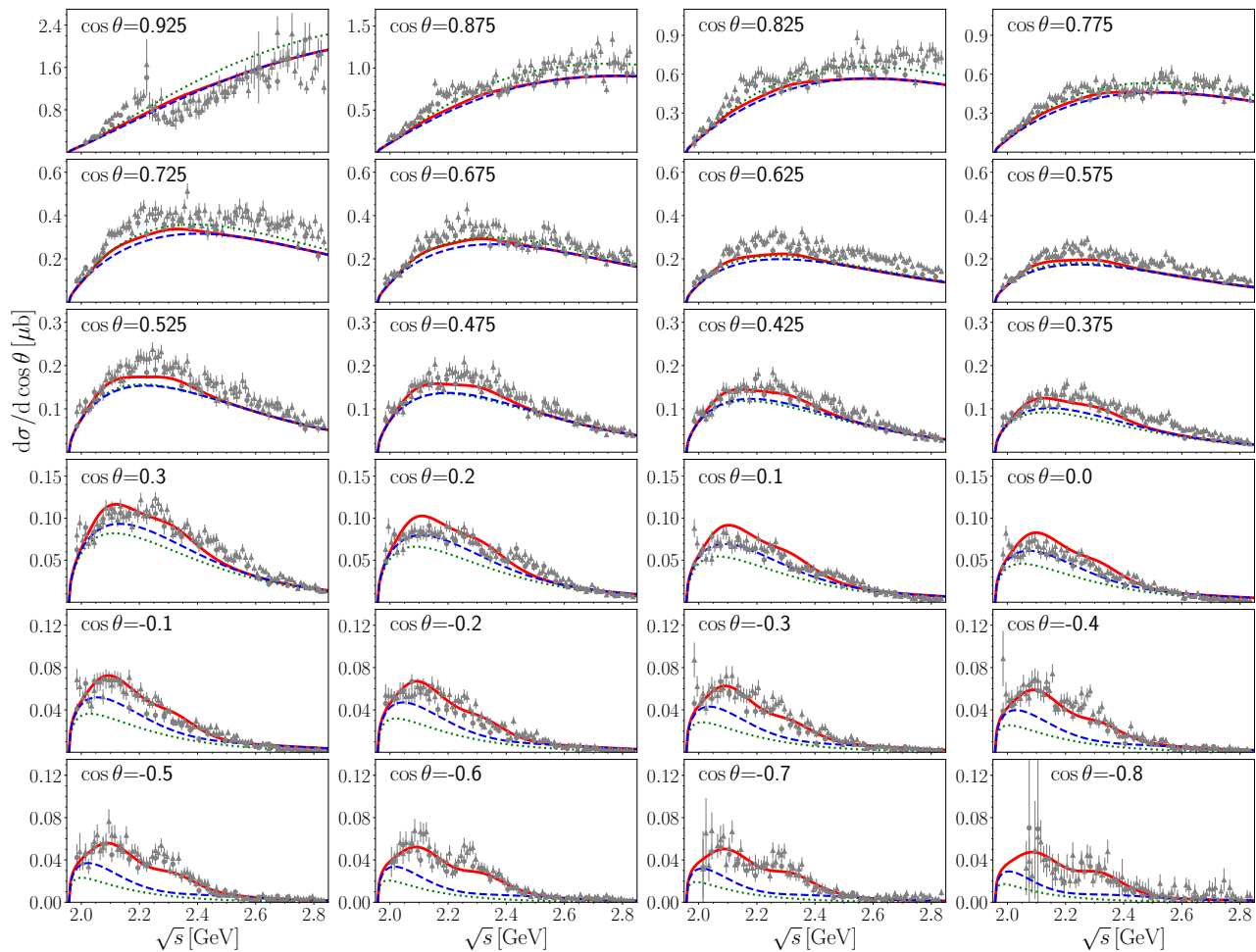


FIG. 4. Differential cross sections  $d\sigma/d\cos\theta$  are plotted as functions of the c.m. energy  $\sqrt{s}$  at full scattering angles. The red solid curves and the blue dashed curves stand for the total contribution and the contribution without  $N^*$ , respectively. The green dotted curves stand for the Pomeron contribution. The CLAS data shown by triangles and circles indicate the charged- and neutral- $K\bar{K}$  decay modes of  $\phi$ , respectively [10].

We depict the differential cross sections as functions of  $\sqrt{s}$  in Fig. 4 for wide scattering-angle regions in comparison to the charged ( $\phi \rightarrow K^+K^-$ ) and neutral ( $\phi \rightarrow K_S^0 K_L^0$ ) decay modes [10], which are shown by the triangle and circle symbols, respectively. The angle  $\theta$  is that of the outgoing  $\phi$ -meson in the c.m. frame. Note that they are very



similar to each other and should be treated as a single data set and not be treated independently because they are related to each other and the systematic uncertainties are greatly reduced [10]. Except for the most forward angle  $\cos\theta = 0.925$ , the total results turn out to be reasonably successful over the wide scattering-angle regions. The ratio of the Pomeron contribution to the CLAS data gradually decreases as  $\cos\theta$  decreases. Note that PS- and S-meson exchanges, respectively, make constructive and destructive interference effects with the dominant Pomeron exchange. In the case of the SDMEs, the opposite interference pattern is observed. As seen in Fig. 3, the contribution of the  $a_0$ -meson exchange is about two times larger than that of the  $\pi$ -meson exchange. Thus we expect the differential cross sections to be rather decreased with the Pomeron plus  $a_0$ - and  $\pi$ -meson exchange model relative to the Pomeron exchange one. Thus we need to include one more ingredient in the  $t$  channel and we select the  $f_1(1285)$  meson trajectory. Its inclusion makes the differential cross sections enhanced to a certain extent. That is why the Born contribution is almost the same as the Pomeron contribution at the intermediate angles and even prevails over it at the backward ones. Nevertheless, the ratio of the Born contribution to the CLAS data at the backward angles  $\cos\theta \lesssim -0.5$  is even less than 50%. Two  $N^*$  contributions improve theoretical results remarkably, i.e., the two peaks around  $\sqrt{s} \approx 2.1$  and 2.3 GeV can be accounted for by the effects of  $N^*(2000, 5/2^+)$  and  $N(2300, 1/2^+)$ , respectively. The clear bump structure at  $\cos\theta = 0.925$  around  $\sqrt{s} \approx 2.2$  GeV, admittedly, may arise from another mechanism, the study of which is beyond the scope of the present work.

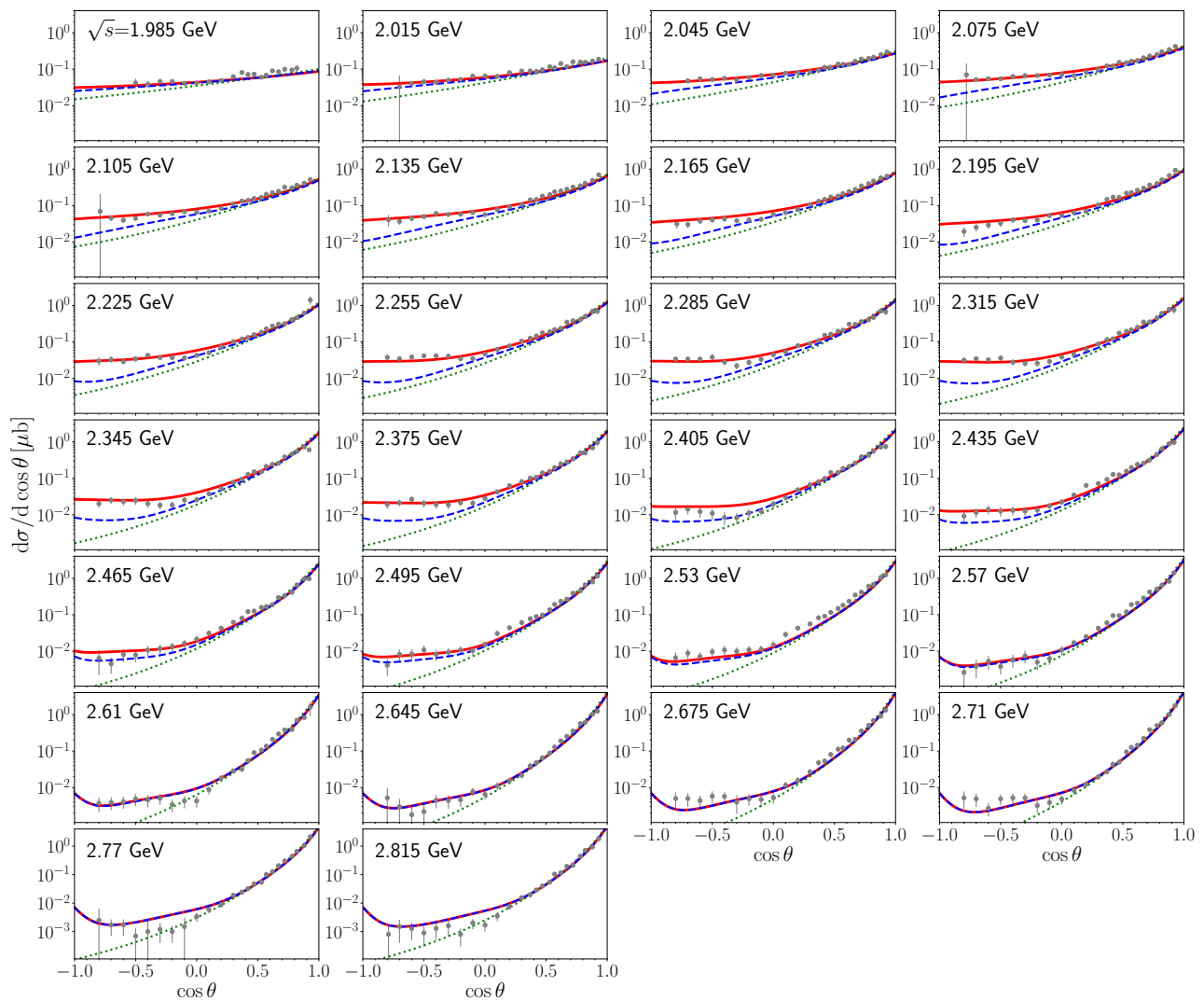


FIG. 5. Differential cross sections  $d\sigma/d\cos\theta$  are plotted as functions of  $\cos\theta$  for different c.m. energies  $\sqrt{s} = (1.985 - 2.815)$  GeV. The curve notations are the same as those in Fig. 4. The CLAS data indicate the neutral- $K\bar{K}$  decay mode of  $\phi$  [10].

The differential cross sections  $d\sigma/d\cos\theta$  are displayed in Fig. 5 as functions of  $\cos\theta$  for different c.m. energy bins in the logarithmic scale. The Pomeron contribution (green dotted curves) governs the forward angle regions, but

starts to deviate from the CLAS data [10] as  $\cos\theta$  decreases. The inclusion of AV-, PS-, and S-meson exchanges (blue dashed curves) makes the curves increased in the region of  $\cos\theta \lesssim 0.5$ . The remaining discrepancies in the range of  $\sqrt{s} = (2.04 - 2.50)$  GeV are reduced by the effects of the  $N^*$  contributions. Consequently, the total results (red solid curves) are in very good agreement with the CLAS data.

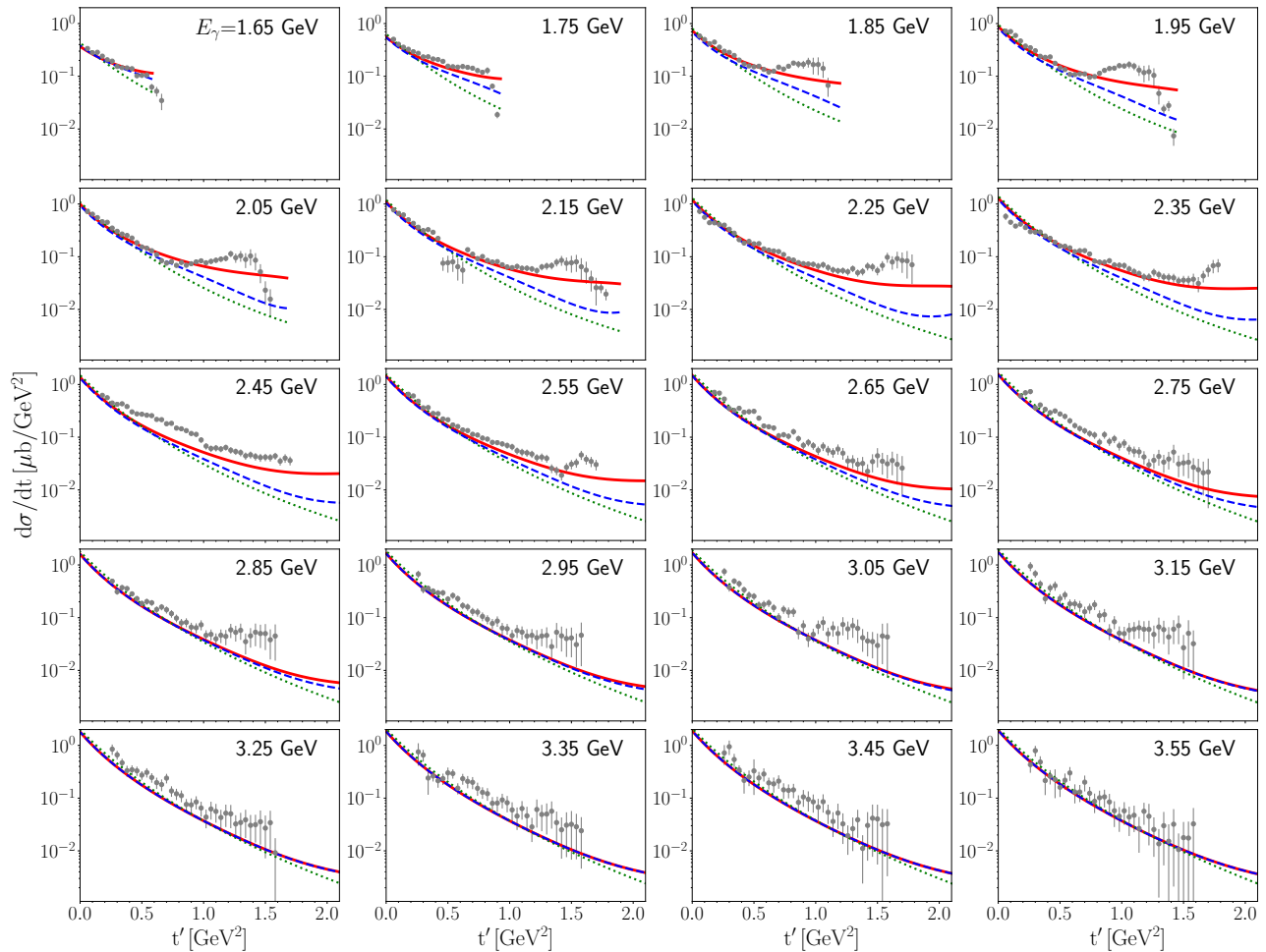


FIG. 6. Differential cross sections  $d\sigma/dt$  are plotted as functions of  $t' \equiv |t - t_{\min}|$  for different laboratory energies  $E_\gamma = (1.65 - 3.55)$  GeV. The curve notations are the same as those in Fig. 4. The CLAS data indicate the neutral- $K\bar{K}$  decay mode of  $\phi$  [9].

In Fig. 6, we present the numerical results of the forward-scattering cross sections  $d\sigma/dt$  as functions of the momentum transfer squared  $t' \equiv |t - t_{\min}|$  for different laboratory energy bins where  $t_{\min}$  indicates the minimum value of  $t$  at a certain fixed energy. The tendency is similar to Fig. 5 in general for the corresponding beam energies. The level of agreement between the total results and the CLAS data [9] is quite good at  $E_\gamma^{\text{lab}} \gtrsim 2.45$  GeV. However, we find the bump structures at large values of  $t'$  near the threshold  $E_\gamma^{\text{lab}} = (1.85 - 2.35)$  GeV, indicating that the  $N^*$  contributions should be treated with caution.

From now on, we present the results of SDMEs [60] in various reference frames to shed light on the relevant reaction mechanism. Their definitions are given in Appendix B. Figure 7 depicts them as a function of  $\sqrt{s}$  at  $\cos\theta = 0.7$  in the Gottfried-Jackson (red dashed curves), Adair (green dot-dashed curves), and helicity (blue solid curves) frames [10]. We observe definitely nonzero values of  $\rho_{00}^0$  in the Gottfried-Jackson and helicity frames, which show that  $t$ -channel (TCHC) and  $s$ -channel (SCHC) helicity conservations are broken, respectively. The diffractive Pomeron exchange is expected to be dominant at the forward-scattering angles, but underestimates the  $\rho_{00}^0$  data in all three frames as depicted in Fig. 7(a). The finite values of  $\rho_{00}^0$  reflect the single helicity-flip transition between the incoming photon and the outgoing  $\phi$  meson from its definition as understood by

$$\rho_{00}^0 \propto |\mathcal{M}_{\lambda_\gamma=1, \lambda_\phi=0}|^2 + |\mathcal{M}_{\lambda_\gamma=-1, \lambda_\phi=0}|^2. \quad (28)$$

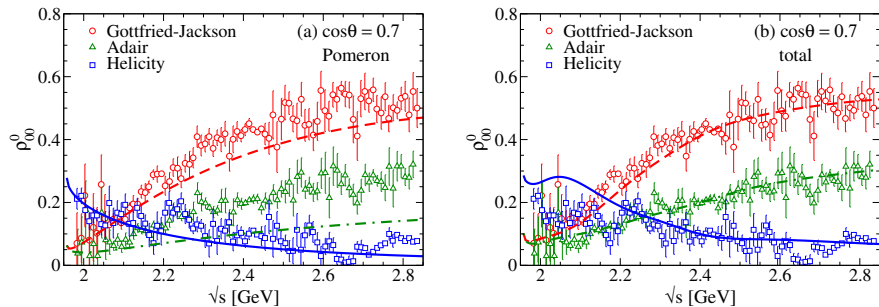


FIG. 7. Spin-density matrix elements  $\rho_{00}^0$  are plotted as functions of  $\sqrt{s}$  at  $\cos\theta = 0.7$  in the three different reference frames. The red dotted, green dot-dashed, and blue solid curves indicate the results in the Gottfried-Jackson, Adair, and helicity frames, respectively, which correspond to the CLAS data (red circles, green triangles, and blue squares) from the charged- $K\bar{K}$  decay mode of  $\phi$  [10]. The results in panels (a) and (b) stand for the Pomeron and total contributions, respectively.

The Pomeron exchange is known as a gluon-rich Regge trajectory with a vacuum quantum number ( $J^{PC} = 0^{++}$ ) and thus we expect TCHC in principle. Moreover, the argument in support of SCHC for diffractive vector meson photoproductions is given in the literature [16, 61]. However, there is no clear reason why TCHC and SCHC should hold for our phenomenological DL model [16]. The total results finally succeed in a satisfactory description of  $\rho_{00}^0$  in all three frames as displayed in the Fig. 7(b). Thus, the relative contributions of AV-, PS-, and S-meson exchanges to the dominant Pomeron contribution are confirmed more explicitly. We can immediately test a simple DL Pomeron plus  $\pi$ - and  $\eta$ -meson exchange model [14] via the present SDME data. It turns out that the agreement between these model predictions and the SDME data is not satisfactory in all three frames. The comparison with the LEPS data also supports this argument as shown in Fig. 6 of Ref. [62].

It is worthwhile to examine other components of SDMEs to understand the effects of the various contributions. Figure 8 depicts  $\rho_{00}^0$  (red circles) and  $\rho_{1-1}^0$  (blue triangles) as functions of  $\sqrt{s}$  at full scattering angles in the Adair frame [10]. It is noticeable that the  $\rho_{00}^0$  data are quite large, unlike the  $\rho_{1-1}^0$  data which are small but finite. The  $\rho_{00}^0$  data are all positive and reveal bumplike structures at the threshold of  $\sqrt{s} = (2.0 - 2.2)$  GeV and backward-scattering angles of  $\cos\theta \lesssim 0.2$ , even though systematical limitations at the angles make the structures unclear. First, we find that the Pomeron exchange alone (red dashed curves) is not sufficient for describing the  $\rho_{00}^0$  data at the forward-scattering angles. The inclusion of the S mesons to the Pomeron exchange makes  $\rho_{00}^0$  increased, but the inclusion of the PS mesons makes the results worse by pulling down  $\rho_{00}^0$ . The cutoff masses in the form factor of Eq. (17) are constrained so as to describe simultaneously the differential cross sections and SDMEs. Second, it turns out that the bumplike structures observed at the backward-scattering angles is a clear evidence of the  $N^*$  contribution. At  $\sqrt{s} = (2.0 - 2.2)$  GeV, both the  $\rho_{00}^0$  data and the total theoretical results (red solid curves) are the strongest at very backward angles, and get reduced steadily with respect to  $\cos\theta$ , and then vanish around  $\cos\theta = 0.2$ . This tendency is almost the same as the numerical results of the differential cross sections in Fig. 4. The Born contribution merely underestimates the  $\rho_{00}^0$  data for all the available energies. The  $N^*(2000, 5/2^+)$  contribution is mainly responsible for the local structures rather than other spin-1/2 and -3/2 nucleon resonances. The total results are in good agreement with the CLAS data in general except in the intermediate-angle region where the interference between the Born and resonant terms is maximal.

Let us continue to present our results in comparison to the LEPS data [62]. The total contribution of various SDMEs are displayed in Figs. 9(a) and 9(b) as functions of  $t' \equiv |t - t_{\min}|$  in the Adair and helicity frames, respectively. Here we examine three different threshold energies, i.e.,  $E_{\gamma}^{lab} = 1.95$  GeV (dotted curves), 2.15 GeV (dashed curves), and 2.35 GeV (solid curves). We find distinctive large values for  $\rho_{1-1}^1$  and  $\text{Im}[\rho_{1-1}^2]$ . Their similar absolute magnitudes are understood from the following relation [15],

$$-\text{Im}[\rho_{1-1}^2] \approx \rho_{1-1}^1 - \frac{(\rho_{1-1}^0)^2}{1 - \rho_{00}^0}, \quad (29)$$

because small values of  $\rho_{1-1}^0$  are experimentally observed. The data other than  $\rho_{1-1}^1$  and  $\text{Im}[\rho_{1-1}^2]$  are almost zero and are in good agreement with our results. The considered region  $t' = (0.0 - 0.2)$  GeV<sup>2</sup> is dominated by the  $t$ -channel exchange process for the differential cross sections but is sensitive to the structure of the  $N^*$  exchange amplitudes for the case of SDMEs.

It is more informative to present our results in the Gottfried-Jackson frame for which we separately show the Pomeron and total contributions in Figs. 10(a) and 10(b), respectively. The increase in the magnitude of  $\rho_{00}^0$  is consistent with the results of Fig. 8. When a double helicity-flip transition is forbidden, the  $\rho_{1-1}^0$  is exactly zero by

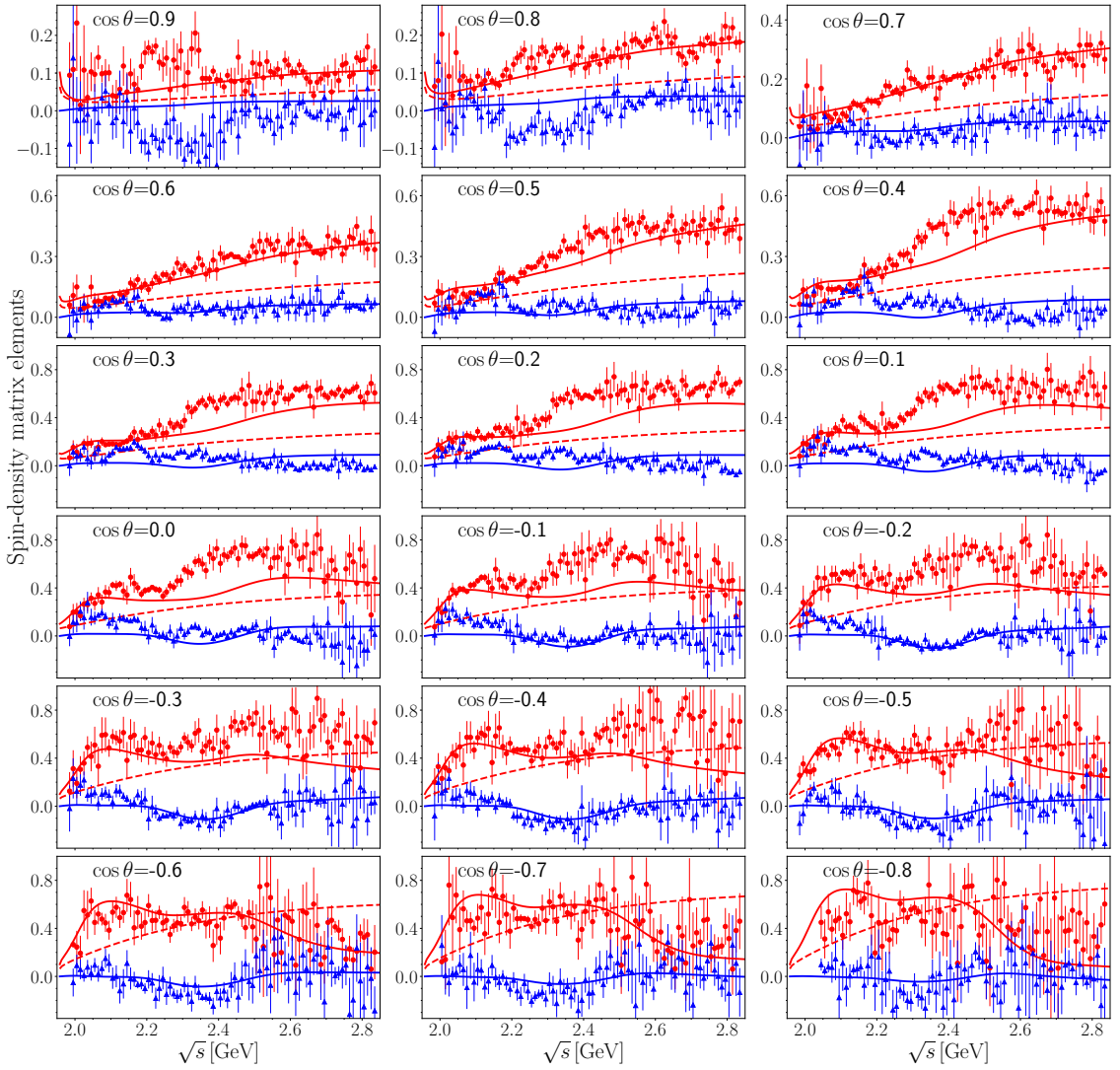


FIG. 8. Spin-density matrix elements  $\rho_{00}^0$  (red circles) and  $\rho_{1-1}^0$  (blue triangles) are plotted as functions of  $\sqrt{s}$  at full scattering angles in the Adair frame. The red dashed curve indicates the results of  $\rho_{00}^0$  for Pomeron exchange, and red solid curves and blue solid curves correspond to the total results of  $\rho_{00}^0$  and  $\rho_{1-1}^0$ , respectively. The CLAS data indicate the charged- $K\bar{K}$  decay mode of  $\phi$  [10].

construction. However, the small but finite value of  $\rho_{1-1}^0$  at large  $t'$  even for Pomeron exchange implies the possible spin-orbital interaction from our modified DL model [14, 62, 63]. For the pure Pomeron exchange process, the following relation [15],

$$\rho_{1-1}^1 \simeq \frac{1}{2}(1 - \rho_{00}^0), \quad (30)$$

also holds and is confirmed by our numerical results. Note that  $\rho_{1-1}^1$  is very interesting, because it allows us to measure the asymmetry of the relative strength between the natural ( $N$ ) and unnatural ( $U$ ) parity exchange processes, and is written as

$$\rho_{1-1}^1 = \frac{1}{2} \frac{\sigma^N - \sigma^U}{\sigma^N + \sigma^U} + \frac{1}{2} \rho_{00}^1. \quad (31)$$

For example, PS- and S-meson exchanges correspond to unnatural and natural parity exchanges, respectively, and no single helicity-flip transition occurs, resulting in  $\rho_{00}^1 = 0$ . Thus we exactly obtain  $\rho_{1-1}^1 = -0.5$  and  $0.5$  for them, respectively. A large deviation of  $\rho_{1-1}^1$  from Pomeron exchange is compensated by the inclusion of AV- and PS-meson

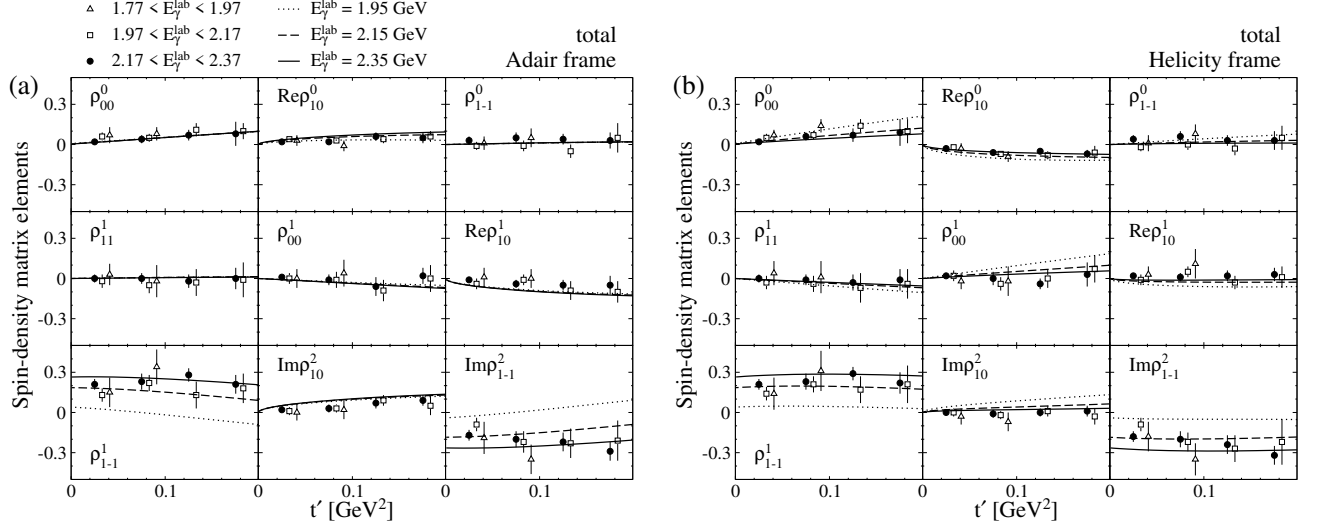


FIG. 9. The total contribution of various spin-density matrix elements are plotted as functions of  $t' \equiv |t - t_{\min}|$  for three different laboratory energies,  $E_{\gamma}^{\text{lab}} = 1.95$  GeV (dotted curves), 2.15 GeV (dashed curves), and 2.35 GeV (solid curves), in the Adair (a) and helicity (b) frames. The data are from the LEPS Collaboration [62].

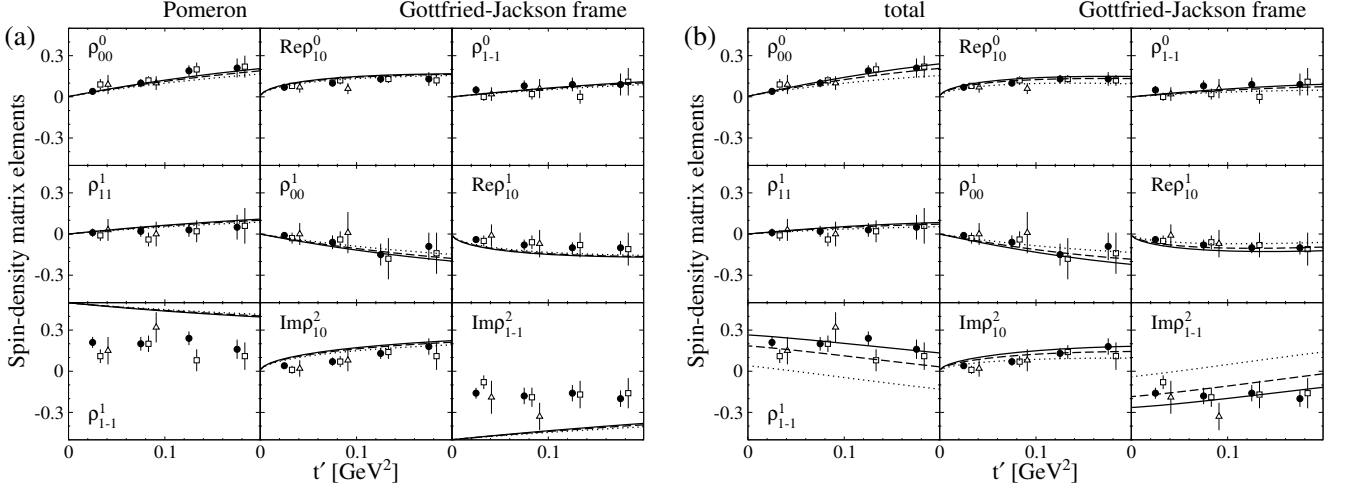


FIG. 10. The same as Fig. 9 but for the Pomeron (a) and total (b) contributions, respectively, in the Gottfried-Jackson frame.

unnatural parity exchanges and the  $N^*$  contribution which involves both natural and unnatural parity exchanges. The direct  $\phi$ -meson radiation hardly affects the SDMEs or the cross sections. The total results are improved in comparison to the results of Pomeron exchange.

Figure 11 shows the results of  $\rho_{00}^0$ ,  $\rho_{10}^0$ , and  $\rho_{1-1}^0$  as functions of  $\cos\theta$  in the Gottfried-Jackson frame for three different threshold energies as done in Figs. 9 and 10. The CLAS energy bins are 10 MeV wide [10], but the LEPS ones much wider, i.e., 200 MeV wide [62]. As expected, the forward-scattering angles are well described by Pomeron exchange. Large discrepancies shown at backward-scattering angles are highly decreased by the inclusion of nucleon resonances, especially for  $\rho_{10}^0$  and  $\rho_{1-1}^0$ .

#### IV. SUMMARY

We have investigated the  $\phi$ -meson photoproduction mechanism for the wide-scattering-angle regions, based on the effective Lagrangian approach in the tree-level Born approximation. As for the Born contribution, we considered the universal Pomeron exchange and the  $f_1(1285)$  axial-vector-meson,  $(\pi, \eta)$  pseudoscalar-meson, and  $(a_0, f_0)$  scalar-meson exchanges, in addition to the direct  $\phi$ -meson radiation contributions. We newly took two nucleon resonances

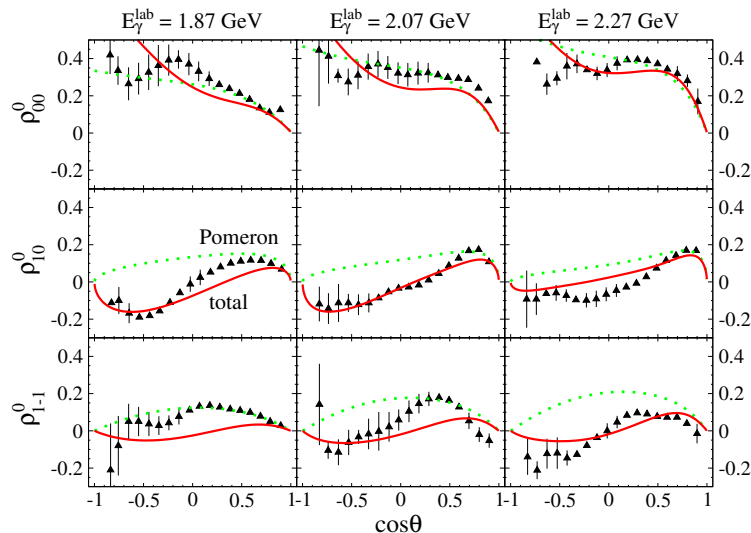


FIG. 11. Spin-density matrix elements  $\rho_{00}^0$ ,  $\rho_{10}^0$ , and  $\rho_{-1-1}^0$  are plotted as functions of  $\cos\theta$  for three different lab. energies in the Gottfried-Jackson frame. The green dotted curves and the red solid curves stand for the Pomeron and total contributions, respectively. The CLAS data indicate the charged- $K\bar{K}$  decay mode of  $\phi$  [10].

from the PDG into account, i.e.,  $N^*(2000, 5/2^+)$  and  $N^*(2300, 1/2^+)$ . We list important observations as follows.

- Pomeron exchange is responsible for the description of the available total cross section data in the intermediate-energy,  $E_\gamma^{\text{lab}} = (3 - 10)$  GeV, and high-energy,  $E_\gamma^{\text{lab}} \gtrsim 30$  GeV, ranges.
- The key point is how to incorporate the AV-, PS-, and S-meson exchanges into the Pomeron contribution to describe the abundant differential cross sections and SDMEs in the low energy region  $\sqrt{s} = (2.0 - 2.8)$  GeV. The  $N^*$  contributions are also essential to account for the two bumplike structures near  $\sqrt{s} \approx 2.1$  and 2.3 GeV shown at the backward-scattering angles.
- According to the interference patterns between the Born and  $N^*$  contributions, the CLAS and LEPS data are reproduced qualitatively well, except for the *dip* or the *peak* structure shown near the threshold in the forward-scattering cross section. We leave the long-standing puzzle on this structure to future work. The role of the PS-meson exchanges is found to be definitely different from that of the S-meson exchanges, and both are essential to describe the cross sections and SDMEs simultaneously together with the AV-meson exchange.
- The  $N^*$  contributions should be dealt with carefully because of the lack of the information on the  $N^* \rightarrow \phi N$  decay channels. We select  $N^*(2000, 5/2^+)$  and  $N^*(2300, 1/2^+)$  from the PDG and extract their branching ratios by the comparison with the CLAS data. We find that the bumplike structures observed in the backward-scattering angles are explained qualitatively well by the  $N^*$  contributions.
- We want to mention that the effect of high-spin meson exchanges such as the  $f'_2(1525)$  tensor-meson [63] is revealed especially on  $\rho_{00}^0$  at forward-scattering angles to some extent. However, we do not show these results because we want to emphasize that the role of AV-, PS-, and S-meson exchanges is sufficient for the purpose of this work.

Consequently, as shown in the present work, our rigorous theoretical analyses on the presently available high-statistics and wide-angle-coverage experimental data for the various physical observables will be valuable for a profound understanding for the light-flavor ( $\rho$  and  $\omega$ ) and hidden-flavor ( $J/\psi$ ) vector meson photoproductions [64–71]. Related works will appear elsewhere.

#### ACKNOWLEDGMENTS

S.i.N. thanks B. Dey, who kindly provided him with the experimental data for the present work. The authors are grateful to A. Hosaka (RCNP, Osaka) and A. I. Titov (JINR, Dubna) for fruitful discussions. This work was supported by the National Research Foundation of Korea (NRF) (Grant No. 2018R1A5A1025563). The work of

S.i.N. was supported in part by a NRF grant (Grant No. 2019R1A2C1005697). The work of S.-H.Kim was supported in part by a NRF grant (Grant No. 2019R1C1C1005790).

## APPENDIX A: INVARIANT AMPLITUDES

The invariant amplitude for  $\gamma p \rightarrow \phi p$  can be written as follows

$$\mathcal{M} = \varepsilon_\nu^* \bar{u}_{N'} \mathcal{M}^{\mu\nu} u_N \epsilon_\mu, \quad (32)$$

where  $\epsilon_\mu$  and  $\varepsilon_\nu$  stand for the polarization vectors for the photon and the  $\phi$  meson, respectively. The Dirac spinors of the incident and outgoing nucleons are denoted by  $u_N$  and  $u_{N'}$ , respectively.

The invariant amplitude for the Pomeron exchange is given by

$$\mathcal{M}_{\mathbb{P}}^{\mu\nu} = -M_{\mathbb{P}}(s, t) \Gamma_{\mathbb{P}}^{\mu\nu}, \quad (33)$$

where the scalar function is

$$M_{\mathbb{P}}(s, t) = C_{\mathbb{P}} F_\phi(t) F_N(t) \frac{1}{s} \left( \frac{s}{s_{\mathbb{P}}} \right)^{\alpha_{\mathbb{P}}(t)} \exp \left[ -\frac{i\pi}{2} \alpha_{\mathbb{P}}(t) \right], \quad (34)$$

and the transition operator is

$$\Gamma_{\mathbb{P}}^{\mu\nu} = \left( g^{\mu\nu} - \frac{k_2^\mu k_2^\nu}{k_2^2} \right) \not{k}_1 - \left( k_1^\nu - \frac{k_2^\nu k_1 \cdot k_2}{k_2^2} \right) \gamma^\mu - \left( \gamma^\nu - \frac{\not{k}_2 k_2^\nu}{k_2^2} \right) k_2^\mu. \quad (35)$$

The energy-scale factors for the Pomeron is given by  $s_{\mathbb{P}} = (M_N + M_\phi)^2$ . Practically, a phenomenological consideration gives a change for the last term of Eq. (35)

$$k_2^\mu \rightarrow k_2^\mu - \frac{(p_1 + p_2)^\mu k_1 \cdot k_2}{(p_1 + p_2) \cdot k_1}, \quad (36)$$

to satisfy the Ward-Takahashi identity in  $\bar{u}_{N'}[\dots]u_N$  of Eq. (32) [15].

The invariant amplitudes for  $f_1(1285)$  axial-vector-,  $(\pi, \eta)$  pseudoscalar-, and  $(a_0, f_0)$  scalar-meson exchanges take the following forms:

$$\mathcal{M}_{f_1}^{\mu\nu} = i \frac{M_\phi^2 g_{\gamma\phi f_1} g_{f_1 NN}}{t - M_{f_1}^2} \epsilon^{\mu\nu\alpha\beta} \left[ -g_{\alpha\lambda} + \frac{q_{t\alpha} q_{t\lambda}}{M_{f_1}^2} \right] \left[ \gamma^\lambda + \frac{\kappa_{f_1 NN}}{2M_N} \gamma^\sigma \gamma^\lambda q_{t\sigma} \right] \gamma_5 k_{1\beta}, \quad (37)$$

$$\mathcal{M}_{\Phi}^{\mu\nu} = i \frac{e}{M_\phi} \frac{g_{\gamma\Phi\phi} g_{\Phi NN}}{t - M_\Phi^2} \epsilon^{\mu\nu\alpha\beta} k_{1\alpha} k_{2\beta} \gamma_5,$$

$$\mathcal{M}_S^{\mu\nu} = \frac{e}{M_\phi} \frac{2g_{\gamma S\phi} g_{S NN}}{t - M_S^2 + i\Gamma_S M_S} (k_1 \cdot k_2 g^{\mu\nu} - k_1^\mu k_2^\nu), \quad (38)$$

where we use  $M_{a_0} = 980$  MeV,  $M_{f_0} = 990$  MeV, and  $\Gamma_{a_0, f_0} = 75$  MeV [13].

The  $\phi$ -radiation invariant amplitudes are constructed as

$$\begin{aligned} \mathcal{M}_{\phi \text{ rad}, s}^{\mu\nu} &= \frac{e g_{\phi NN}}{s - M_N^2} \left( \gamma^\nu - i \frac{\kappa_{\phi NN}}{2M_N} \sigma^{\nu\alpha} k_{2\alpha} \right) (\not{q}_s + M_N) \left( \gamma^\mu + i \frac{\kappa_N}{2M_N} \sigma^{\mu\beta} k_{1\beta} \right), \\ \mathcal{M}_{\phi \text{ rad}, u}^{\mu\nu} &= \frac{e g_{\phi NN}}{u - M_N^2} \left( \gamma^\mu + i \frac{\kappa_N}{2M_N} \sigma^{\mu\alpha} k_{1\alpha} \right) (\not{q}_u + M_N) \left( \gamma^\nu - i \frac{\kappa_{\phi NN}}{2M_N} \sigma^{\nu\beta} k_{2\beta} \right), \end{aligned} \quad (39)$$

for the  $s$  and  $u$  channels, respectively.  $q_{t,s,u}$  are the four momenta of the exchanged particles, i.e.,  $q_t = k_2 - k_1$ ,  $q_s = k_1 + p_1$ , and  $q_u = p_2 - k_1$ .

The invariant amplitudes for exchanges of spin-1/2 and -5/2 resonances are computed as

$$\begin{aligned} \mathcal{M}_{N^*, 1/2^\pm}^{\mu\nu} &= \frac{-ie}{s - M_{N^*}^2 + i\Gamma_{N^*} M_{N^*}} \frac{h_1}{(2M_N)^2} \left[ g_1 \frac{M_\phi^2}{M_{N^*} \mp M_N} \Gamma^{\nu(\mp)} \mp i g_2 \Gamma^{(\mp)} \sigma^{\nu\beta} k_{2\beta} \right] (\not{q}_s + M_{N^*}) \Gamma^{(\mp)} \sigma^{\mu\alpha} k_{1\alpha}, \\ \mathcal{M}_{N^*, 5/2^\pm}^{\mu\nu} &= e \left[ \frac{g_1}{(2M_N)^2} \Gamma_\rho^{(\mp)} + \frac{g_2}{(2M_N)^3} p_{2\rho} \Gamma^{(\mp)} - \frac{g_3}{(2M_N)^3} k_{2\rho} \Gamma^{(\mp)} \right] k_2^{\beta_2} (k_2^{\beta_1} g^{\nu\rho} - k_2^\rho g^{\nu\beta_1}) \Delta_{\beta_1 \beta_2; \alpha_1 \alpha_2}(q_s) \\ &\quad \times \left[ \frac{h_1}{(2M_N)^2} \Gamma_\delta^{(\mp)} \mp \frac{h_2}{(2M_N)^3} \Gamma^{(\mp)} p_{1\delta} \right] k_2^{\alpha_2} (k_1^{\alpha_1} g^{\mu\delta} - k_1^\delta g^{\alpha_1 \mu}), \end{aligned} \quad (40)$$

for the  $s$ -channel diagram. The propagator of a spin-5/2 baryon field is represented as [72]

$$\begin{aligned} \Delta_{\beta_2\beta_1;\alpha_2\alpha_1}(q) &= \frac{\not{q} + M_{N^*}}{s - M_{N^*}^2 + i\Gamma_{N^*}M_{N^*}} \\ &\times \left[ \frac{1}{2}(\bar{g}_{\beta_1\alpha_1}\bar{g}_{\beta_2\alpha_2} + \bar{g}_{\beta_1\alpha_2}\bar{g}_{\beta_2\alpha_1}) - \frac{1}{5}\bar{g}_{\beta_1\beta_2}\bar{g}_{\alpha_1\alpha_2} - \frac{1}{10}(\bar{\gamma}_{\beta_1}\bar{\gamma}_{\alpha_1}\bar{g}_{\beta_2\alpha_2} + \bar{\gamma}_{\beta_1}\bar{\gamma}_{\alpha_2}\bar{g}_{\beta_2\alpha_1} + \bar{\gamma}_{\beta_2}\bar{\gamma}_{\alpha_1}\bar{g}_{\beta_1\alpha_2} + \bar{\gamma}_{\beta_2}\bar{\gamma}_{\alpha_2}\bar{g}_{\beta_1\alpha_1}) \right], \end{aligned} \quad (41)$$

with

$$\bar{g}_{\alpha\beta} = g_{\alpha\beta} - \frac{q_\alpha q_\beta}{M_{N^*}^2}, \quad \bar{\gamma}_\alpha = \gamma_\alpha - \frac{q_\alpha}{M_{N^*}} \not{q}. \quad (42)$$

## APPENDIX B: SPIN-DENSITY MATRIX ELEMENTS

The spin-density matrix elements (SDMEs) can be expressed in terms of the helicity amplitudes [60]:

$$\begin{aligned} \rho_{\lambda\lambda'}^0 &= \frac{1}{N} \sum_{\lambda_\gamma, \lambda_i, \lambda_f} \mathcal{M}_{\lambda_f\lambda; \lambda_i\lambda_\gamma} \mathcal{M}_{\lambda_f\lambda'; \lambda_i\lambda_\gamma}^*, \\ \rho_{\lambda\lambda'}^1 &= \frac{1}{N} \sum_{\lambda_\gamma, \lambda_i, \lambda_f} \mathcal{M}_{\lambda_f\lambda; \lambda_i-\lambda_\gamma} \mathcal{M}_{\lambda_f\lambda'; \lambda_i\lambda_\gamma}^*, \\ \rho_{\lambda\lambda'}^2 &= \frac{i}{N} \sum_{\lambda_\gamma, \lambda_i, \lambda_f} \lambda_\gamma \mathcal{M}_{\lambda_f\lambda; \lambda_i-\lambda_\gamma} \mathcal{M}_{\lambda_f\lambda'; \lambda_i\lambda_\gamma}^*, \\ \rho_{\lambda\lambda'}^3 &= \frac{1}{N} \sum_{\lambda_\gamma, \lambda_i, \lambda_f} \lambda_\gamma \mathcal{M}_{\lambda_f\lambda; \lambda_i\lambda_\gamma} \mathcal{M}_{\lambda_f\lambda'; \lambda_i\lambda_\gamma}^*, \end{aligned} \quad (43)$$

where the normalization factor  $N$  is defined as

$$N = \sum |\mathcal{M}_{\lambda_f\lambda; \lambda_i\lambda_\gamma}|^2. \quad (44)$$

The helicity states for the incoming photon and nucleon and the outgoing nucleon are denoted by  $\lambda_\gamma$ ,  $\lambda_i$ , and  $\lambda_f$ , respectively, whereas  $\lambda$  and  $\lambda'$  stand for those for the outgoing  $\phi$  meson. By the symmetry property, the helicity amplitudes have

$$\mathcal{M}_{-\lambda_f-\lambda; -\lambda_i-\lambda_\gamma} = (-1)^{(\lambda-\lambda_f)-(\lambda_\gamma-\lambda_i)} \mathcal{M}_{\lambda_f\lambda; \lambda_i\lambda_\gamma}. \quad (45)$$

We have the following relations:

$$\begin{aligned} \rho_{\lambda\lambda'}^\alpha &= (-1)^{\lambda-\lambda'} \rho_{-\lambda-\lambda'}^\alpha \quad \text{for } \alpha = 0, 1, \\ \rho_{\lambda\lambda'}^\alpha &= -(-1)^{\lambda-\lambda'} \rho_{-\lambda-\lambda'}^\alpha \quad \text{for } \alpha = 2, 3. \end{aligned} \quad (46)$$

There is an ambiguity in choosing the quantization axis when computing the SDMEs because they are not Lorentz-invariant quantities. Thus the spin-quantization direction for the  $\phi$  meson must be determined. We choose the Adair (A) frame, the helicity (H) frame, and the Gottfried-Jackson (GJ) frame. Figures 12(a) and 12(b) are schematic diagrams in the c.m. frame and in the  $\phi$ -meson rest frame, respectively. In the Adair frame, the  $z$  axis is parallel to the incoming photon momentum in the c.m. frame. The helicity and Gottfried-Jackson frames are when  $z$  axis is antiparallel to the momentum of the outgoing nucleon or is chosen to be parallel to that of the incoming photon, respectively. The former and latter ones are in favor of the  $s$ -channel and  $t$ -channel helicity conservations, respectively. When the SDMEs are given in one frame, it is straightforward to derive them in other frames by a Wigner rotation. The rotation angles are expressed as [10, 60]

$$\begin{aligned} \alpha_{A \rightarrow H} &= \theta_{\text{c.m.}}, \\ \alpha_{H \rightarrow GJ} &= -\cos^{-1} \left( \frac{v - \cos \theta_{\text{c.m.}}}{v \cos \theta_{\text{c.m.}} - 1} \right), \\ \alpha_{A \rightarrow GJ} &= \alpha_{A \rightarrow H} + \alpha_{H \rightarrow GJ}, \end{aligned} \quad (47)$$



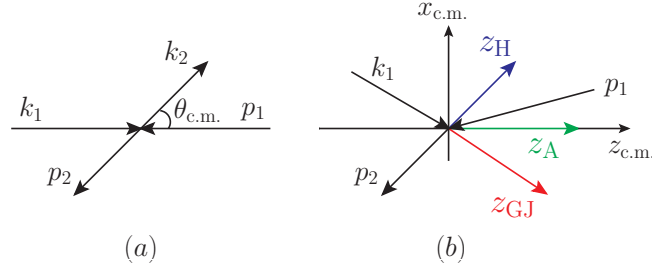


FIG. 12. Schematic diagrams for  $\gamma p \rightarrow \phi p$  in (a) the center-of-mass (c.m.) frame and (b) the  $\phi$ -meson rest frame. A (green), H (blue), and GJ (red) stand for the Adair, helicity and Gottfried-Jackson frames, respectively.

where  $v$  is the velocity of the  $K$  meson in the  $\phi$ -meson rest frame (for the  $\phi \rightarrow K\bar{K}$  decay).

- 
- [1] T. Mibe *et al.* (LEPS Collaboration), Phys. Rev. Lett. **95**, 182001 (2005).  
[2] S. Okubo, Phys. Lett. **5**, 165 (1963).  
[3] G. Zweig, CERN Reports, CERN-TH-401 and CERN-TH-412, 1964.  
[4] J. Iizuka, Prog. Theor. Phys. Suppl. **37**, 21 (1966).  
[5] S. Ozaki, A. Hosaka, H. Nagahiro, and O. Scholten, Phys. Rev. C **80**, 035201 (2009); **81**, 059901 (E) (2010).  
[6] H. Y. Ryu, A. I. Titov, A. Hosaka, and H.-C. Kim, Prog. Theor. Exp. Phys. **2014**, 023D03 (2014).  
[7] A. Kiswandhi, J. J. Xie, and S. N. Yang, Phys. Lett. B **691**, 214 (2010).  
[8] A. Kiswandhi and S. N. Yang, Phys. Rev. C **86**, 015203 (2012); **86**, 019904 (E) (2012).  
[9] H. Seraydaryan *et al.* (CLAS Collaboration), Phys. Rev. C **89**, 055206 (2014).  
[10] B. Dey *et al.* (CLAS Collaboration), Phys. Rev. C **89**, 055208 (2014); **90**, 019901 (A) (2014).  
[11] S. Y. Ryu *et al.* (LEPS Collaboration), Phys. Rev. Lett. **116**, 232001 (2016).  
[12] B. Dey, arXiv:1403.3730.  
[13] M. Tanabashi *et al.* (Particle Data Group), Phys. Rev. D **98**, 030001 (2018).  
[14] A. I. Titov, T.-S. H. Lee, H. Toki, and O. Streltsova, Phys. Rev. C **60**, 035205 (1999).  
[15] A. I. Titov and T. S. H. Lee, Phys. Rev. C **67**, 065205 (2003).  
[16] A. Donnachie and P. V. Landshoff, Nucl. Phys. **B244**, 322 (1984); **267**, 690 (1986); Phys. Lett. B **185**, 403 (1987).  
[17] M. A. Pichowsky and T. S. H. Lee, Phys. Lett. B **379**, 1 (1996).  
[18] M. A. Pichowsky and T. S. H. Lee, Phys. Rev. D **56**, 1644 (1997).  
[19] A. Donnachie and P. V. Landshoff, Nucl. Phys. **B311**, 509 (1989).  
[20] J. M. Laget and R. Mendez-Galain, Nucl. Phys. A **581**, 397 (1995).  
[21] G. A. Jaroszkiewicz and P. V. Landshoff, Phys. Rev. D **10**, 170 (1974).  
[22] A. Donnachie and P. V. Landshoff, Nucl. Phys. **B231**, 189 (1984).  
[23] N. I. Kochelev, D. P. Min, Y. Oh, V. Vento, and A. V. Vinnikov, Phys. Rev. D **61**, 094008 (2000).  
[24] N. Kaiser and U. G. Meissner, Nucl. Phys. **A519**, 671 (1990).  
[25] M. Birkel and H. Fritzsche, Phys. Rev. D **53**, 6195 (1996).  
[26] A. Donnachie *et al.*, *Pomeron Physics and QCD* (Cambridge University, Cambridge, England, 2002).  
[27] M. M. Brisudova, L. Burakovsky, and T. Goldman, Phys. Rev. D **61**, 054013 (2000).  
[28] V. G. J. Stoks and Th. A. Rijken, Phys. Rev. C **59**, 3009 (1999).  
[29] Th. A. Rijken, V. G. J. Stoks, and Y. Yamamoto, Phys. Rev. C **59**, 21 (1999).  
[30] U. G. Meissner, V. Mull, J. Speth, and J. W. van Orden, Phys. Lett. B **408**, 381 (1997).  
[31] K. Ohta, Phys. Rev. C **40**, 1335 (1989).  
[32] H. Haberzettl, Phys. Rev. C **56**, 2041 (1997).  
[33] H. Haberzettl, C. Bennhold, T. Mart, and T. Feuster, Phys. Rev. C **58**, R40 (1998).  
[34] R. M. Davidson and R. Workman, Phys. Rev. C **63**, 025210 (2001).  
[35] H. Haberzettl, X. Y. Wang, and J. He, Phys. Rev. C **92**, 055503 (2015).  
[36] Y. Oh, J. Korean Phys. Soc. **59**, 3344 (2011).  
[37] S.-H. Kim, S.-i. Nam, A. Hosaka, and H.-C. Kim, Phys. Rev. D **88**, 054012 (2013).  
[38] W. Rarita and J. Schwinger, Phys. Rev. **60**, 61 (1941).  
[39] V. Shklyar, H. Lenske, U. Mosel, and G. Penner, Phys. Rev. C **71**, 055206 (2005); **72**, 019903 (E) (2005).  
[40] Y. Oh, C. M. Ko, and K. Nakayama, Phys. Rev. C **77**, 045204 (2008).  
[41] A. V. Anisovich *et al.* (CLAS Collaboration), Phys. Lett. B **771**, 142 (2017).  
[42] Q. Zhao, J. P. Didelez, M. Guidal, and B. Saghai, Nucl. Phys. **A660**, 323 (1999).  
[43] Q. Zhao, B. Saghai, and J. S. Al-Khalili, Phys. Lett. B **509**, 231 (2001).

- [44] R. F. Lebed, Phys. Rev. D **92**, 114030 (2015).
- [45] R. Aaij *et al.* (LHCb Collaboration), Phys. Rev. Lett. **115**, 072001 (2015).
- [46] R. Aaij *et al.* (LHCb Collaboration), Phys. Rev. Lett. **122**, 222001 (2019).
- [47] V. Kubarovsky and M. B. Voloshin, Phys. Rev. D **92**, 031502(R) (2015).
- [48] Q. Wang, X. H. Liu, and Q. Zhao, Phys. Rev. D **92**, 034022 (2015).
- [49] M. Karliner and J. L. Rosner, Phys. Lett. B **752**, 329 (2016).
- [50] A. N. Hiller Blin, C. Fernández-Ramírez, A. Jackura, V. Mathieu, V. I. Mokeev, A. Pilloni, and A. P. Szczepaniak, Phys. Rev. D **94**, 034002 (2016).
- [51] S.-H. Kim, S.-i. Nam, D. Jido, and H.-C. Kim, Phys. Rev. D **96**, 014003 (2017).
- [52] S.-H. Kim and H.-C. Kim, Phys. Lett. B **786**, 156 (2018).
- [53] J. M. Suh, S.-H. Kim, and H.-C. Kim, Phys. Rev. D **99**, 074010 (2019).
- [54] T. Corthals, J. Ryckebusch, and T. Van Cauteren, Phys. Rev. C **73**, 045207 (2006).
- [55] L. De Cruz, J. Ryckebusch, T. Vrancx, and P. Vancraeyveld, Phys. Rev. C **86**, 015212 (2012).
- [56] J. Ballam *et al.*, Phys. Rev. D **7**, 3150 (1973).
- [57] D. P. Barber *et al.*, Z. Phys. C **12**, 1 (1982).
- [58] R. M. Egloff *et al.*, Phys. Rev. Lett. **43**, 657 (1979).
- [59] J. Busenitz *et al.*, Phys. Rev. D **40**, 1 (1989).
- [60] K. Schilling, P. Seyboth, and G. E. Wolf, Nucl. Phys. **B15**, 397 (1970); **B18**, 332 (E) (1970).
- [61] F. J. Gilman, J. Pumplin, A. Schwimmer, and L. Stodolsky, Phys. Lett. **B31**, 387 (1970).
- [62] W. C. Chang *et al.* (LEPS Collaboration), Phys. Rev. C **82**, 015205 (2010).
- [63] J. M. Laget, Phys. Lett. B **489**, 313 (2000).
- [64] K. Mizutani *et al.* (LEPS Collaboration), Phys. Rev. C **96**, 062201 (2017).
- [65] M. Battaglieri *et al.* (CLAS Collaboration), Phys. Rev. Lett. **87**, 172002 (2001).
- [66] C. Wu *et al.*, Eur. Phys. J. A **23**, 317 (2005).
- [67] M. Williams *et al.* (CLAS Collaboration), Phys. Rev. C **80**, 065208 (2009).
- [68] M. Williams *et al.* (CLAS Collaboration), Phys. Rev. C **80**, 065209 (2009).
- [69] V. Vegna *et al.* (GRAAL Collaboration), Phys. Rev. C **91**, 065207 (2015).
- [70] A. Wilson *et al.* (CBELSA and TAPS Collaborations), Phys. Lett. B **749**, 407 (2015).
- [71] P. Collins *et al.* (CLAS Collaboration), Phys. Lett. B **773**, 112 (2017).
- [72] S. J. Chang, Phys. Rev. **161**, 1308 (1967).